



Delft University of Technology

Ultra-high energy spectral prompt PET

Ghosh, S.; Cosmi, V.; Ramakers, R.M.; Beekman, F.J.; Goorden, M.C.

DOI

[10.1088/1361-6560/adbfd7](https://doi.org/10.1088/1361-6560/adbfd7)

Publication date

2025

Document Version

Final published version

Published in

Physics in Medicine and Biology

Citation (APA)

Ghosh, S., Cosmi, V., Ramakers, R. M., Beekman, F. J., & Goorden, M. C. (2025). Ultra-high energy spectral prompt PET. *Physics in Medicine and Biology*, 70(7), Article 075010. <https://doi.org/10.1088/1361-6560/adbfd7>

Important note

To cite this publication, please use the final published version (if applicable). Please check the document version above.

Copyright

Other than for strictly personal use, it is not permitted to download, forward or distribute the text or part of it, without the consent of the author(s) and/or copyright holder(s), unless the work is under an open content license such as Creative Commons.

Takedown policy

Please contact us and provide details if you believe this document breaches copyrights. We will remove access to the work immediately and investigate your claim.

PAPER • OPEN ACCESS

Ultra-high energy spectral prompt PET

To cite this article: Satyajit Ghosh *et al* 2025 *Phys. Med. Biol.* **70** 075010

View the [article online](#) for updates and enhancements.

You may also like

- [Sulfur Effect on Corrosion Behavior of Fe-20Cr-\(Mn, Si\) and Fe-20Ni-20Cr-\(Mn, Si\) in CO₂-H₂O at 650°C](#)
Chun Yu, Thuan Dinh Nguyen, Jianqiang Zhang *et al.*
- [Identifying vulnerability factors associated with heatwave mortality: A spatial statistical analysis across Europe](#)
Benedetta Sestito, Lena Reimann, Maurizio Mazzoleni *et al.*
- [Dareplane: a modular open-source software platform for BCI research with application in closed-loop deep brain stimulation](#)
Matthias Dold, Joana Pereira, Bastian Sajonz *et al.*



PAPER

Ultra-high energy spectral prompt PET

OPEN ACCESS

RECEIVED
28 November 2024REVISED
24 February 2025ACCEPTED FOR PUBLICATION
12 March 2025PUBLISHED
25 March 2025

Original content from
this work may be used
under the terms of the
[Creative Commons
Attribution 4.0 licence](#).

Any further distribution
of this work must
maintain attribution to
the author(s) and the title
of the work, journal
citation and DOI.

Satyajit Ghosh^{1,*} , Valerio Cosmi¹ , Ruud M Ramakers^{1,2}, Freek J Beekman^{1,3} and Marlies C Goorden¹ ¹ Department of Radiation Science and Technology, Delft University of Technology, Delft, The Netherlands² MILabs B.V., Heidelberglaan 100, 3584 CX Utrecht, The Netherlands³ Free Bee International, Gouda, The Netherlands

* Author to whom any correspondence should be addressed.

E-mail: S.Ghosh-1@tudelft.nl**Keywords:** sub-mm resolution, positron range, PET-SPECT, multi-isotope PET, pinhole imagingSupplementary material for this article is available [online](#)**Abstract**

Objective. Utilizing prompt gammas in preclinical pinhole-collimated positron emission tomography (PET) avoids image degradation due to positron range blurring and photon down scatter, enables multi-isotope PET and can improve counting statistics for low-abundance positron emitters. This was earlier reported for ^{124}I , ^{89}Zr and simultaneous $^{124}\text{I} - ^{18}\text{F}$ PET using the VECTor scanner (MILabs, The Netherlands), demonstrating sub-mm resolution despite long positron ranges. The aim of the present study is to investigate if such sub-mm PET imaging is also feasible for a large variety of other isotopes including those with extremely high energy prompt gammas (>1 MeV) or with complex emission spectra of prompt gammas. **Approach.** We use Monte Carlo simulations to assess achievable image resolutions and uniformity across a broad range of spectrum types and emitted prompt gamma energies (603 keV–2.2 MeV), using ^{52}Mn , ^{94}Tc , ^{89}Zr , ^{44}Sc , ^{86}Y , ^{72}As , ^{124}I , ^{38}K , and ^{66}Ga . **Main results.** Our results indicate that sub-millimeter resolution imaging may be feasible for almost all isotopes investigated, with the currently used cluster pinhole collimators. At prompt gamma energies of 603 keV of ^{124}I , an image resolution of ~ 0.65 mm was achieved, while for emissions at 703, 744, 834, and 909 keV of ^{94}Tc , ^{52}Mn , ^{72}As , and ^{89}Zr , respectively, ~ 0.7 mm resolution was obtained. Finally, at ultra-high energies of 1.2 (^{44}Sc) and 1.4 MeV (^{52}Mn) resolutions of ~ 0.75 mm and ~ 0.8 mm could still be achieved although ring artifacts were observed at the highest energies (1.4 MeV). For ^{38}K (2.2 MeV), an image resolution of 1.2 mm was achieved utilizing its 2.2 MeV prompt emission. **Significance.** This work shows that current cluster pinhole collimators are suitable for sub-mm resolution prompt PET up till at least 1.4 MeV. This may open up new avenues to developing new tracer applications and therapies utilizing these PET isotopes.

1. Introduction

Among the numerous modalities employed in small animal imaging, dedicated positron emission tomography (PET) and single photon emission computed tomography (SPECT) scanners are widely utilized. Many different radioisotopes have been employed and investigated with these scanners, facilitating the studies of various diseases, tracer molecules and therapies (Crişan *et al* 2022). Most often PET imaging operates by detecting pairs of annihilation photons ('coincidence PET'), whereas SPECT and some recently developed preclinical PET devices rely on the detection of single gammas, including prompts.

The image quality of coincidence PET is isotope-dependent and relies on factors such as positron range and the emission spectrum. The range over which a positron travels before the generation of 511 keV annihilation photons occurs (positron ranges: table 1) imposes a fundamental limit on the achievable image resolution (Levin and Hoffman 1999). This is particularly problematic in preclinical PET, where resolution requirements are stringent due to the small size of anatomical structures in mice and images get easily compromised, both quantitatively and visually. While using information on the positron range kernel and

Table 1. Half-lives, positron ranges (Evans and Evans 1955), positron emission probabilities, prompt gamma energies (with emission probabilities), and medical applications of studied PET isotopes.

Isotope	$T_{1/2}$	Positron range (Mean)	Positron range (Max)	Positron emission probability	Prompt gamma energy and emission probability	Example of application
^{18}F	109.77 m	0.64 mm	2.27 mm	96.73%	n.a.	FDG-PET (Glaudemans <i>et al</i> 2013)
^{52}Mn	5.59 d	0.58 mm	1.99 mm	29.4%	744 keV (90%), 936 keV (94.5%), 1434 keV (100%)	immunoPET (Graves <i>et al</i> 2015), bone scanning (Topping <i>et al</i> 2013)
^{94}Tc	293 m	0.85 mm	3.15 mm	10.5%	703 keV (99.6%), 850 + 871 keV (195.6%)	
^{89}Zr	78.41 h	0.96 mm	3.61 mm	22.74%	909 keV (99.04%)	immunoPET (Pandya <i>et al</i> 2019)
^{44}Sc	3.97 h	1.68 mm	6.64 mm	94.28%	1157 keV (99.89%)	prostate cancer (Eppard <i>et al</i> 2017)
^{86}Y	14.74 h	1.73 mm	6.86 mm	31.9%	1077 + 1153 keV (113%)	Theranostic pair of ^{90}Y (Rosch <i>et al</i> 1996)
^{72}As	26 h	3.24 mm	12.8 mm	87.8%	834 keV (81%)	immunoPET (Jennewein <i>et al</i> 2008)
^{124}I	4.18 d	3.28 mm	12.9 mm	22.7%	603 keV (62.9%)	Thyroid cancer (Jentzen <i>et al</i> 2008)
^{38}K	7.64 m	3.39 mm	13.4 mm	99.53%	2167 keV (99.85%)	Myocardial perfusion (Duboc <i>et al</i> 1991)
^{66}Ga	9.49 h	5.16 mm	19.8 mm	57%	1039 keV (37%)	Prostate cancer (Rinne <i>et al</i> 2021)

accurate tissue boundaries during image reconstruction can partially mitigate image degradation, it remains a challenge in many instances *e.g.* due to the long tail of the positron range kernel (table 1). Another image degrading effect may occur for PET isotopes that co-emit one or more high energy prompt gammas of sufficient intensities, the probability of which can exceed the positron emission probability by more than an order of magnitude (table 1). These prompt gammas can contaminate the 511 keV photopeak through down scatter, complicating the use of 511 keV gammas for imaging (Lubberink and Herzog 2011, Anizan *et al* 2012, Rosar *et al* 2021). Although various scatter correction methods have been proposed, such as uniform background subtraction (Lubberink *et al* 2002), sinogram tail fitting (Walrand *et al* 2003), and scaled randoms sinogram subtraction (Lubberink 2001), further efforts are necessary to resolve the issue fully (Conti and Eriksson 2016).

Preclinical SPECT systems primarily employ pinhole collimation to benefit from high magnification effects that can be obtained in small animals. Significant advancements have been made to adapt pinhole collimation for high energy imaging (Beekman 2011, 2022) which made these systems also suitable for PET and simultaneous PET-SPECT imaging. This was demonstrated for the ‘Versatile Emission Computed Tomography’ (VECTor) PET-SPECT scanner equipped with proprietary high energy cluster pinhole collimation technology (Beekman 2011, Goorden *et al* 2013) in which pinholes are organized into clusters of pinholes with small opening angles to reduce blurring due to edge penetration. In a recent experimental study (Beekman *et al* 2021), VECTor demonstrated imaging of ^{124}I and ^{89}Zr in phantoms and mice by utilizing their prompt gammas of 603 keV and 909 keV, respectively, resulting in positron-range free images without down scatter contamination (Beekman *et al* 2021). The scanner achieved a conservative estimate of image resolution of 0.75 mm for both ^{89}Zr and ^{124}I (Beekman *et al* 2021). Additionally, simultaneous ^{124}I – ^{18}F PET with excellent separation of isotopes and high quantitative accuracy was demonstrated.

One of the aims of this simulation-based work is to investigate if this concept can be extended to a much wider range of PET isotopes by investigating a series of PET isotopes that have interesting applications but that face challenges when imaging their distributions because they suffer from long positron ranges, low probability of positron emissions and/or down scatter (table 1). For all isotopes, we utilized both annihilation and prompt gammas for imaging to determine which emission provided the optimal image resolution and uniformity for each isotope. Furthermore we assess the deterioration in image quality associated with increasing gamma energy (>1 MeV). Different PET isotopes— ^{52}Mn , ^{94}Tc , ^{89}Zr , ^{44}Sc , ^{86}Y , ^{72}As , ^{124}I , ^{38}K , and ^{66}Ga —were selected for this study to address the aforementioned objectives, with ^{18}F included for comparison. Both image resolution and uniformity were studied for relevant gamma emissions of the isotopes.

Table 2. Comparison between experimental and simulated energy resolutions (E_{res}).

Source	Energy (keV)	Experiment E_{res} (%)	Simulated E_{res} (%)
^{22}Na	511	9.7 (Villena <i>et al</i> 2010)	9.0
^{124}I	603	8.11 (Chris Kamphuis 2024)	8.29
^{89}Zr	909	7.18 (Chris Kamphuis 2024)	6.75

2. Materials and methods

2.1. Scanner description

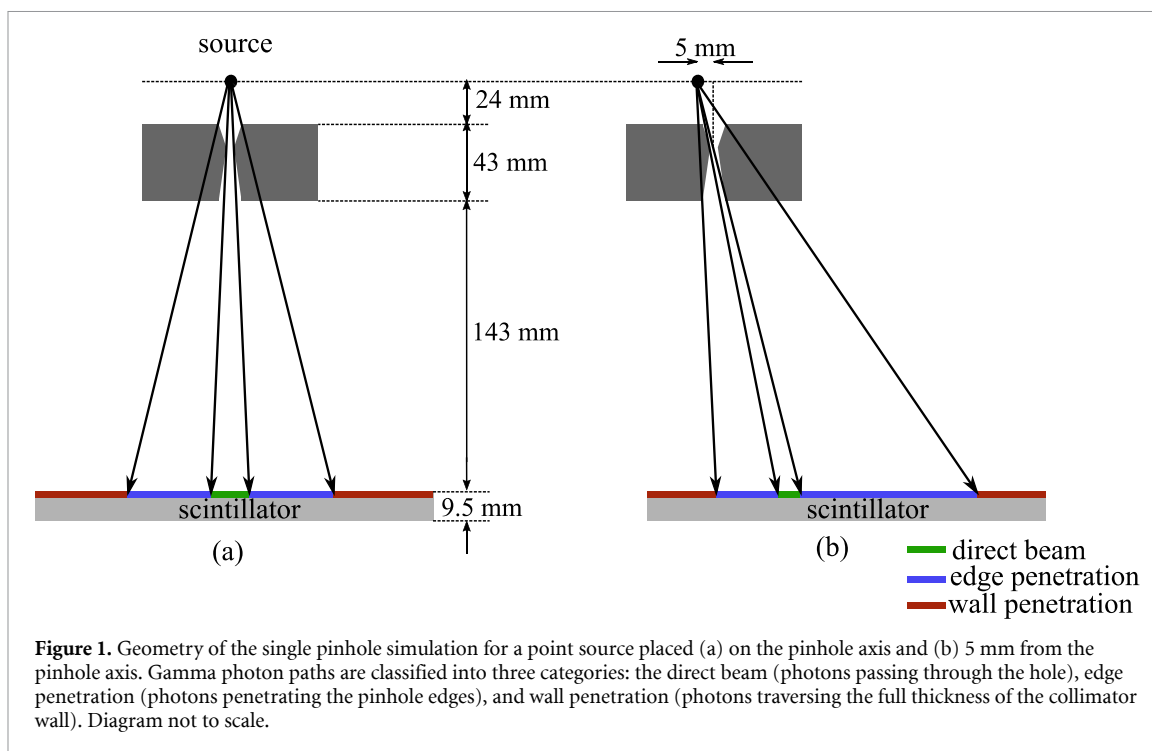
The VECTor scanner simulated in the present study is equipped with a triangular set up of PMT-based monolithic NaI(Tl) scintillator detectors, each with an area of $497 \times 411 \text{ mm}^2$ and standardly a crystal thickness of 9.5 mm. The tungsten collimator comprises 162 pinholes, each with a diameter of 0.7 mm. The original design of the cluster collimator for the VECTor scanner included 192 pinholes; however, only 162 pinholes were utilized for image reconstruction. This is due to some of the pinholes not projecting onto the detector, owing to gaps between the three triangular detectors. The pinholes are arranged in 2×2 clusters (Beekman 2011). These clusters are grouped into four side-by-side rings in the cylindrical collimator (Goorden *et al* 2013). The full opening angle for the pinholes in the inner two rings populated with clusters is 18° , while for the outer two rings, it is 16° , ensuring uniform coverage of pinhole projections on the detector surfaces. The collimator has an inner diameter of 48 mm, a length of 190 mm, and a wall thickness of 43 mm. The centers of all pinholes are defined at a diameter of 64 mm. A specific portion of the field-of-view (FOV), referred to as the central FOV (CFOV), is sampled collectively by all pinhole clusters. It has an approximate diameter of 12 mm and a longitudinal length of 9 mm. The CFOV experiences complete data sampling (satisfies Tuy's conditions Tuy 1983) in a single bed position and this area is readily increased up to the entire body when the bed is translated through the collimator. Data is then acquired from all bed positions ('Scanning Focus Method' Vastenhouw and Beekman 2007) after which all data is utilized jointly in image reconstruction (as detailed in 'Image Reconstruction' section of Vastenhouw and Beekman 2007).

2.2. Monte Carlo simulations

Monte Carlo (MC) simulations were conducted using GATE v9.0 (Jan *et al* 2004), which is based on Geant4 v10.05 (Agostinelli *et al* 2003). The simulations were executed on a CentOS 7.0 cluster utilizing 216 processors concurrently. All relevant physics processes were included in the simulation using the 'emstandard' physics list builder, as described in the GATE documentation. The NaI scintillator detectors of the scanner were modeled as rectangular boxes with dimensions $497 \times 411 \times 9.5 \text{ mm}^3$. The events in which gamma photons lose energy due to multiple interactions within the detector were processed using GATE's 'adder' digitizer module. In this module, the energies from different interactions are summed, and the position is determined as the energy-weighted centroid of the interaction points. The light guides and PMTs of the detector were not directly simulated; instead, their effects were implicitly simulated as a post-processing step. This was done by assuming an energy resolution of 9% at 511 keV and an intrinsic spatial resolution of 3.5 mm, in accordance with the specifications provided by the manufacturer. The energy resolution at other energies was scaled using a $1/\sqrt{E}$ proportionality relation, which approximates the experimentally determined energy resolution values at various gamma energies (table 2, Sibczynski *et al* 2017). These resolutions were implemented by sampling from Gaussian distributions. All post-processing tasks were performed using in-house MATLAB scripts. The detector electronics of the current VECTor scanner are optimized for gamma acquisition up to 1.2 MeV. For this simulation-based study, we assumed that the scanner can be accurately calibrated to a maximum energy of 2.3 MeV (2.2 MeV being the highest energy in our study). MC simulations were both done for a single pinhole and for a full VECTor scanner as detailed below.

2.2.1. Single pinhole simulation

To assess the extent of edge penetration for different energies, we conducted MC simulations to obtain the point spread function (PSF) of a single pinhole. PSFs were generated for a point source placed both on the pinhole axis and 5 mm off-axis (figure 1). The geometrical parameters of the simulation were chosen to be conform to those of the VECTor scanner: the distance between the point source and the inner wall of the collimator was 24 mm, while the pinhole-to-detector distance was 178 mm. The pinhole, with a diameter of 0.7 mm, was positioned at the center of a tungsten rectangular slab with a thickness of 43 mm. Depending on photon travel paths, photon interaction positions in the detector plane can be classified into three regions—the direct beam, edge penetration, and wall penetration, depicted in green, blue, and red,



respectively, in figure 1. Direct beam photons are considered to be those that pass through the hole, while edge penetration photons traverse the pinhole edges. In instances of wall penetration, photons pass through the full thickness of the collimator wall. In practice, the boundaries between these regions are not completely distinct due to the intrinsic spatial resolution of the detector and Compton scattering from pinhole edges. Additionally, in the actual VECTor scanner, the relative positions and orientations of pinholes and the detector are different for different pinholes. Despite this complexity, we believe that our simplified simulated experiment captures the major variations of the PSFs.

For computational efficiency, a gamma pencil beam with an angular width of 40° was directed towards the line connecting source position and pinhole center. Various gamma energies were tested,—140, 511, 603, 744, 834, 909 keV, 1.0, 1.2, 1.4, 2.2 MeV. These energies correspond to those of the annihilation and prompt gamma energies emitted by the isotopes considered in this work except for 140 keV, which is the standard energy for SPECT imaging and therefore chosen for comparison. The photopeak energy windows used for these gamma energies are the same as those used in the phantom simulations (table 3). In each simulation, a total of 10^{10} emitted gammas was simulated.

2.2.2. Scanner simulation and data acquisition

Additional to single pinhole simulations, a MC simulation of the full VECTor scanner was conducted. Among the three detectors, the first detector was oriented perpendicular to the y -axis and translated to coordinates (0, -215 mm, 0). The second and third detectors were rotated by $\pm 120^\circ$ around the z -axis and translated to (-186 mm, -107 mm, 0) and (186 mm, -107 mm, 0), respectively, to accurately represent the triangular geometry of the VECTor scanner. The multi-pinhole cluster collimator was defined in the simulation based on the geometry parameters provided by the manufacturer. The materials used in the collimator were tungsten (97%), iron (1.5%), and nickel (1.5%). The pinholes were modeled as two conical cylinders facing each other.

A total of nine PET isotopes— ^{52}Mn , ^{94}Tc , ^{89}Zr , ^{44}Sc , ^{86}Y , ^{72}As , ^{124}I , ^{38}K , ^{68}Ga —were considered (see table 1). The selection of isotopes was based on factors such as possible biomedical applications, prompt gamma emission energies (up to 2.2 MeV for scanner characterization), and their relevance to studying down scatter issues unique to certain isotopes, e.g. ^{68}Ga , ^{89}Zr . The standard PET isotope ^{18}F was included for comparison. The isotopes were defined as ‘ion sources’ to simulate all possible emissions with their correct intensities. Three-dimensional photon interaction locations in the NaI(Tl) crystal were then used to generate detector projections, which were sampled on a 1.072×1.072 mm² pixel grid, matching the pixel size of the detector used in the VECTor scanner. Projections from both annihilation gamma and available prompt gamma emission(s) of sufficient intensity were acquired for each isotope based on the photopeak windows provided in table 3.

2.2.3. Digital phantoms

A Derenzo resolution phantom containing rods with diameters of 0.6, 0.65, 0.7, 0.75, 0.8, and 0.85 mm, each with a height of 10 mm, was employed in this study. The phantom was assumed to be made of PMMA cylinder of diameter 20 mm and height 12 mm. The activity concentration was set to 250 MBq ml⁻¹ for all isotopes, and the scan duration was set to one hour. All possible types of emissions from the isotopes were simulated. Due to the phantom's dimensions exceeding the CFOV of the scanner, data acquisition was performed using a multiplanar trajectory (MPT) (Vaissier *et al* 2012) over 9 bed positions. The MPT scheme was selected to guarantee sufficient sampling of the object, achieved by employing a conservatively high number of bed positions per plane. For ³⁸K, in addition to the first Derenzo resolution phantom, a second phantom with rod diameters of 0.9, 1.0, 1.1, 1.2, 1.3, and 1.4 mm was employed to assess resolution. This was necessary because no rod sectors were resolved in the first Derenzo phantom for this isotope.

For uniformity studies, a cylindrical water phantom with a diameter of 20 mm and a height of 15 mm, containing a uniform activity concentration of 5 MBq ml⁻¹, was used. The scan duration was kept at the same value as for the Derenzo phantom (1 h). The scan was conducted using a spiral trajectory (Vaissier *et al* 2012) over 17 bed positions. The use of a spiral trajectory reduces scan time compared to a MPT, without compromising image quality (Vaissier *et al* 2012).

2.2.4. Uniformity phantom analysis

Uniformity was calculated using six circular ROIs with a radius of 1.5 mm, measured across five axial slices with a slice thickness of 2 voxels each, where voxel size was 0.4 mm. Percentage uniformity was defined as the ratio of the standard deviation (σ) to the mean (μ), averaged over all six ROIs and the five axial slices

$$\text{Uniformity (\%)} = \frac{\sigma}{\mu} * 100\%. \quad (1)$$

2.2.5. Positron range simulations

Positron annihilation point distributions for the PET isotopes under study were generated through MC simulations; a point source was placed at the center of a 20 cm water sphere and five million annihilation point coordinates were recorded for each isotope. The probability of annihilation within each voxel of a 31 × 31 × 31 voxel grid was stored, with the center of the central voxel in the grid corresponding to the point source position. The voxel size was set to 0.4 mm, matching the reconstructed image voxel size.

The use of an effectively infinite water medium to generate positron range kernels is an approximation. A more accurate model would involve using the actual three-dimensional distribution of the different materials present in the phantom.

2.3. Image reconstruction

Image reconstruction was conducted utilizing the dual-matrix dual-voxel similarity regulated ordered-subset expectation maximization (DM-DV-SROSEM) algorithm (Kamphuis *et al* 1997) which was also used in experimental studies. SROSEM (Vaissier *et al* 2016) resembles OSEM but dynamically adapts the number of subsets used based on the similarity of update terms across different subsets. In our implementation, a maximum of 128 pixel-based subsets (Branderhorst *et al* 2010) was employed, with a similarity threshold set at 40%. A cutoff of 1% was applied to the forward projectors, meaning that gammas traveling paths with a probability of less than 1% of penetrating the collimator were not included (Goorden *et al* 2016). Following the DM framework (Kamphuis *et al* 1997), unmatched backprojectors were employed with a higher cutoff value of 20%, facilitating faster convergence without compromising image quality. To further accelerate reconstruction, the DV approach was adopted (Goorden *et al* 2020). In this approach, forward matrices were divided into a central part with fine voxel binning and a slowly varying tail part with rougher binning (twice the voxel size). Positron range correction (PRC) was implemented by iteratively convolving the activity distribution with the positron range kernel during the forward projection step of the reconstruction process. Comparisons were made between the 511 keV reconstructions with and without PRC. Notably, image reconstruction from prompt emissions does not require PRC, as prompt gammas are emitted directly from the isotope.

Energy-dependent system matrices were computed for all necessary energies using a ray-tracing software (Goorden *et al* 2011, 2016). This ray-tracing code accounts for attenuation through the collimator and detector but does not include scatter. However, the scatter component of the projection, captured using the triple energy window technique (Ogawa *et al* 1991), was incorporated in image reconstruction to compensate for the absence of a scatter contribution in the matrices. In the 1.4 and 2.2 MeV reconstructions, instead of 1%, 3% and 5% cutoff forward matrices were used, respectively, to reduce ring artifacts (more in sections 2.4 and 3.6). Additionally, multi-photopeak imaging of closely spaced prompt gamma pairs, 850 + 871 keV for ⁹⁴Tc and 1077 + 1153 keV for ⁸⁶Y, was performed using system matrices at intensity-weighted gamma

energies. For ^{94}Tc , the intensity-weighted gamma energy of the 850 + 871 keV photopeak is 861 keV, whereas for ^{86}Y , the corresponding energy of the 1077 + 1153 keV photopeak is 1096 keV.

The original reconstructed images have dimensions of $76 \times 76 \times 26$, with a voxel size of 0.4 mm. For improved visualization, ten central layers along the transaxial dimension were summed, and the obtained 76×76 images were redefined on a finer 256×256 grid using MATLAB's 'resize' function which applies bicubic interpolation. All images were subsequently smoothed using a 0.5 mm FWHM Gaussian kernel. For comparison, all isotope images were scaled to activity concentration units (MBq ml^{-1}). Both positron range-corrected and uncorrected 511 keV images from each isotope were obtained for comparative analysis. All prompt gamma emissions with adequate intensities were utilized individually for image reconstruction. The maximum achievable resolution for each isotope was determined through a visual comparison of all Derenzo resolution phantom images.

2.4. Effect of different tail cut off in ultra-high energy imaging

In Goorden *et al* (2016) it was demonstrated that using the same tail cutoff for the forward projections (20%), as employed in 140 keV reconstructions for the same system, does not yield high-quality images for 511 keV. This is attributed to the fact that gamma photon paths with a probability of less than 20% of penetrating the collimator edges, which belong to the tail part of the PSF, constitute a significant portion of the photon flux at gamma energies of 511 keV (see figure 3 of Goorden *et al* 2016). Hence, simulating this tail in system matrix calculation is essential for high energy imaging. It was found that a cutoff of 1% provided a good trade-off between image quality and reconstruction time (Goorden *et al* 2016). Given that we are imaging ultra-high energy gamma emissions (>1 MeV) for the first time, it is crucial to investigate the effect of cutoff on imaging performance. To this end, we generated system matrices with cutoffs ranging from 1% to 7% for ultra-high energies of 1.4 and 2.2 MeV. The reconstructed resolution images using these different matrices were then analyzed. To minimize computation time, only the 1% and 3% matrices were utilized for the analysis of uniformity phantom images.

3. Results

3.1. PSFs for a single pinhole

The line profiles of PSFs for the single pinhole are presented in figure 2. The plot is segmented into three distinct regions: a segment consisting of direct photons, a segment with photons that penetrated through the pinhole edges, and a part containing photons that penetrated through the collimator wall, as defined in section 2.2.1. As anticipated, the amount of pinhole edge penetration increases with higher gamma energies. Notably, at ultra-high energies (>1 MeV), significant penetration through the entire 43 mm thickness of the collimator (wall penetration) was observed at considerable distances from the pinhole axis. Both edge and wall penetrations are more pronounced for the off-axis source position (figure 2(b)). It is suggested that wall penetration from adjacent pinholes can accumulate and significantly contribute to system matrices. These effects undoubtedly broaden PSFs at ultra-high energies, thereby probably making the image reconstruction problem more underdetermined. The percentage of photons passing through the 43 mm collimator wall without any interaction was calculated using the Beer–Lambert law (Barrett and Swindell 1981) for the gamma energies of interest (table S1 of supplementary material).

3.2. Phantom simulation

The energy spectra of all ten PET isotopes under study, derived from the first 1 mins of acquisition data from resolution phantom simulations, are presented in figure 3. Collimator and detector scatter contributions are also included. Here, the detector scatter contribution refers to events involving at least one Compton scatter event within the detector, while none occurs in the collimator. For some isotopes, higher energy gamma emissions may be detected into the photopeak windows of lower energy gamma emissions due to Compton scattering within the phantom, collimator edges, or detector crystal, a phenomenon denoted by down scatter. Our simulations revealed a negligible contribution from phantom scatter. As an example, for ^{72}As , approximately 1.42% of counts within the photopeak window (table 3) for 511 keV and approximately 0.26% within the photopeak window for 834 keV originate from phantom scatter. Scattering of higher energy gamma rays from the collimator pinhole edges can also significantly contribute to the signal in the photopeak of lower energy gamma rays as is clear from figure 3. For example, down scatter from 2190 keV and 2752 keV gamma rays can contribute to the photopeak of the 1039 keV gamma ray of ^{66}Ga (figure 3). Depending on the relative distance between the higher energy gamma and photopeak of interest, this may result in severely misplaced counts on the detector plane due to the selective contribution from higher angle scatter. Consequently, this effect may degrade image quality (more in section 3.4).

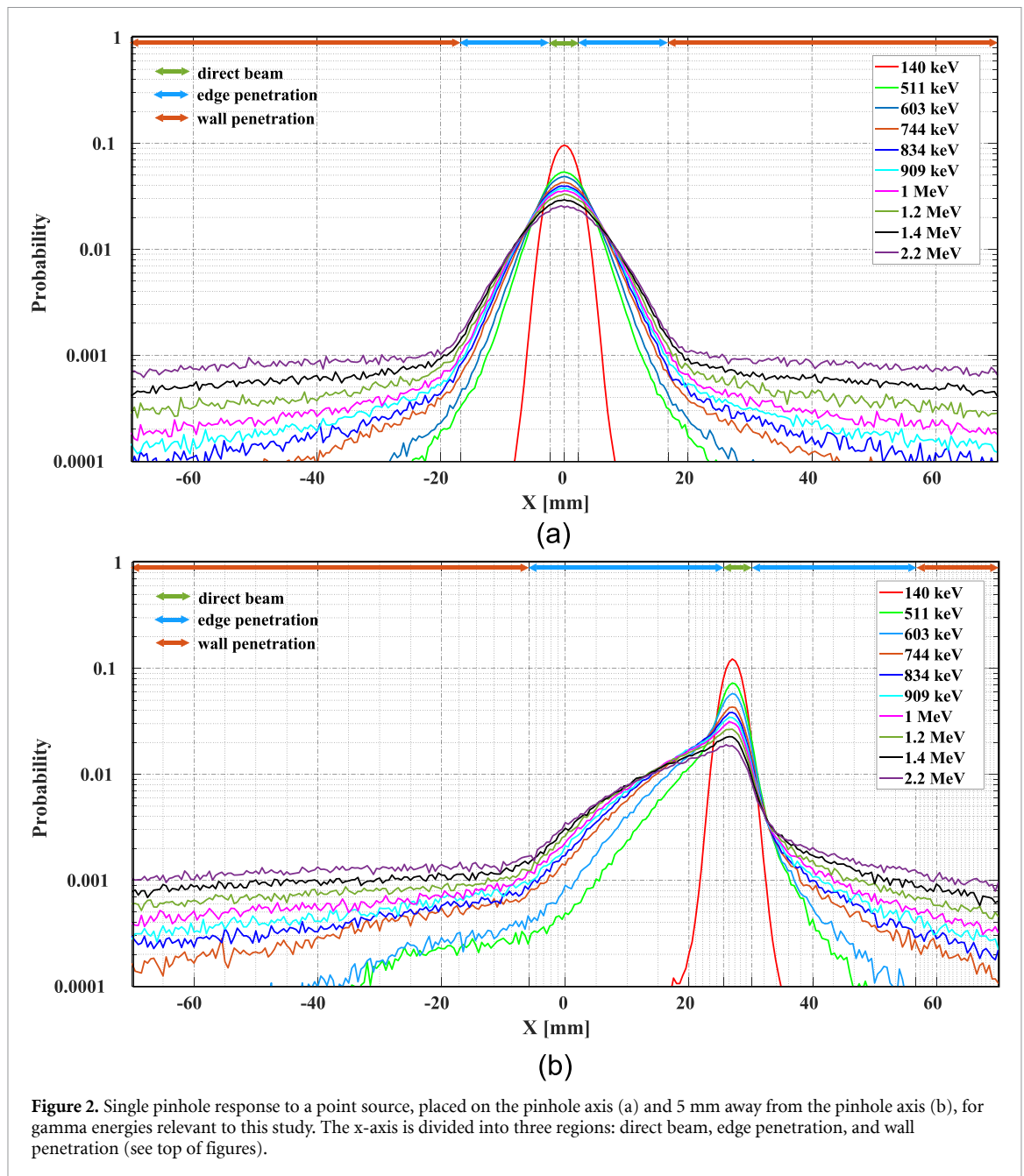


Figure 2. Single pinhole response to a point source, placed on the pinhole axis (a) and 5 mm away from the pinhole axis (b), for gamma energies relevant to this study. The x-axis is divided into three regions: direct beam, edge penetration, and wall penetration (see top of figures).

For all isotopes, photopeak and background windows were selected through visual inspection of spectra (figure 3) and reported in table 3. Many of the isotopes studied in our paper exhibit small to medium intensity gamma emissions near 511 keV, such as 443 keV (17%) for ^{86}Y , 603 keV (63%) for ^{124}I , and 630 keV (8%) for ^{72}As . To avoid including counts from these additional gamma emissions and to maximize the counts within the 511 keV photopeak window, the selected 511 keV photopeak windows for some isotopes are slightly different. For isotopes such as ^{94}Tc and ^{86}Y , adjacent unresolved gamma emissions were reconstructed using a single photopeak window.

3.3. Positron range

Line profiles of the generated positron range kernels for all isotopes are presented in the supplementary material (figure S1). The positron range for various PET isotopes has been extensively studied, both experimentally (Cho *et al* 1975, Derenzo 1979) and through simulations (Le Loirec and Champion 2007a, 2007b, 2007c, Cal-González *et al* 2013). However, most reported results are two-dimensional projections of the original three-dimensional distribution of annihilation points, making them unsuitable for direct use in our study. To validate our simulation, we compared our results with values reported in the literature (see appendix A.1).

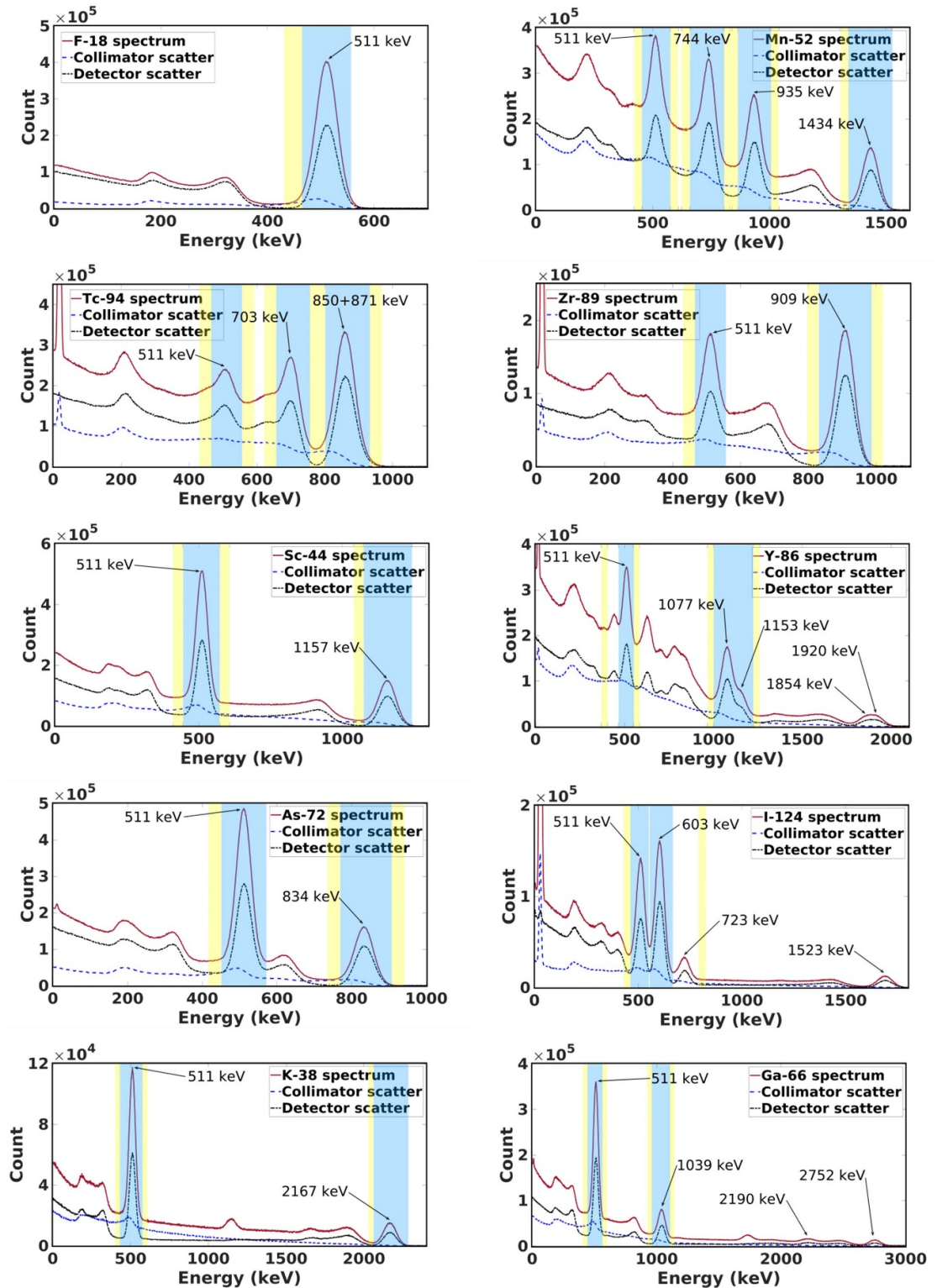


Figure 3. Energy spectra of PET isotopes used in this study: ^{18}F , ^{52}Mn , ^{94}Tc , ^{89}Zr , ^{44}Sc , ^{86}Y , ^{72}As , ^{124}I , ^{38}K and ^{66}Ga , including the photopeak and background energy windows in blue and yellow, respectively. The collimator and detector down scatter spectra are also presented.

3.4. Resolution studies

Resolution phantom images obtained from both the 511 keV and all prompt gamma emissions of sufficient intensity for all isotopes under study are shown in figures 4 and 5. Images were presented at three different iteration numbers: the 50th, 100th, and 180th iteration. Based on visual assessment, a resolution of ~ 0.65 mm is achievable for imaging ^{124}I utilizing its 603 keV prompt gamma emission. Similarly, resolutions of ~ 0.7 mm are attainable for ^{94}Tc , ^{52}Mn , ^{72}As , and ^{89}Zr using their respective prompt gamma emissions at 703 keV, 744 keV, 834 keV, and 909 keV. Furthermore, prompt gamma emissions at ultra-high energies of

Table 3. Photopeak and background energy windows used.

Isotope	Peak energy (keV)	Photopeak window (keV)	Background window-1 (keV)	Background window-2 (keV)
¹⁸ F	511	465–557	430–465	n.a.
⁵² Mn	511	455–575	420–455	575–610
	744	660–805	625–660	805–840
	936	865–1005	830–865	1005–1040
	1434	1340–1525	1305–1340	n.a.
⁹⁴ Tc	511	465–557	430–465	557–592
	703	657–766	622–657	766–801
	850 + 871	791–933	756–791	933–968
⁸⁹ Zr	511	465–557	430–465	n.a.
	909	831–986	796–831	986–1021
⁴⁴ Sc	511	445–573	410–445	573–608
	1157	1074–1242	1039–1074	n.a.
⁸⁶ Y	511	467–550	369–404	550–585
	1077 + 1153	1000–1225	965–1000	1225–1260
⁷² As	511	445–570	410–445	907–942
	834	757–907	722–757	907–942
¹²⁴ I	511	463–551	428–463	790–825
	603	554–667	790–825	n.a.
³⁸ K	511	433–575	398–433	575–610
	2167	2064–2284	2029–2064	n.a.
⁶⁶ Ga	511	445–566	410–445	566–601
	1039	960–1107	925–960	1107–1142

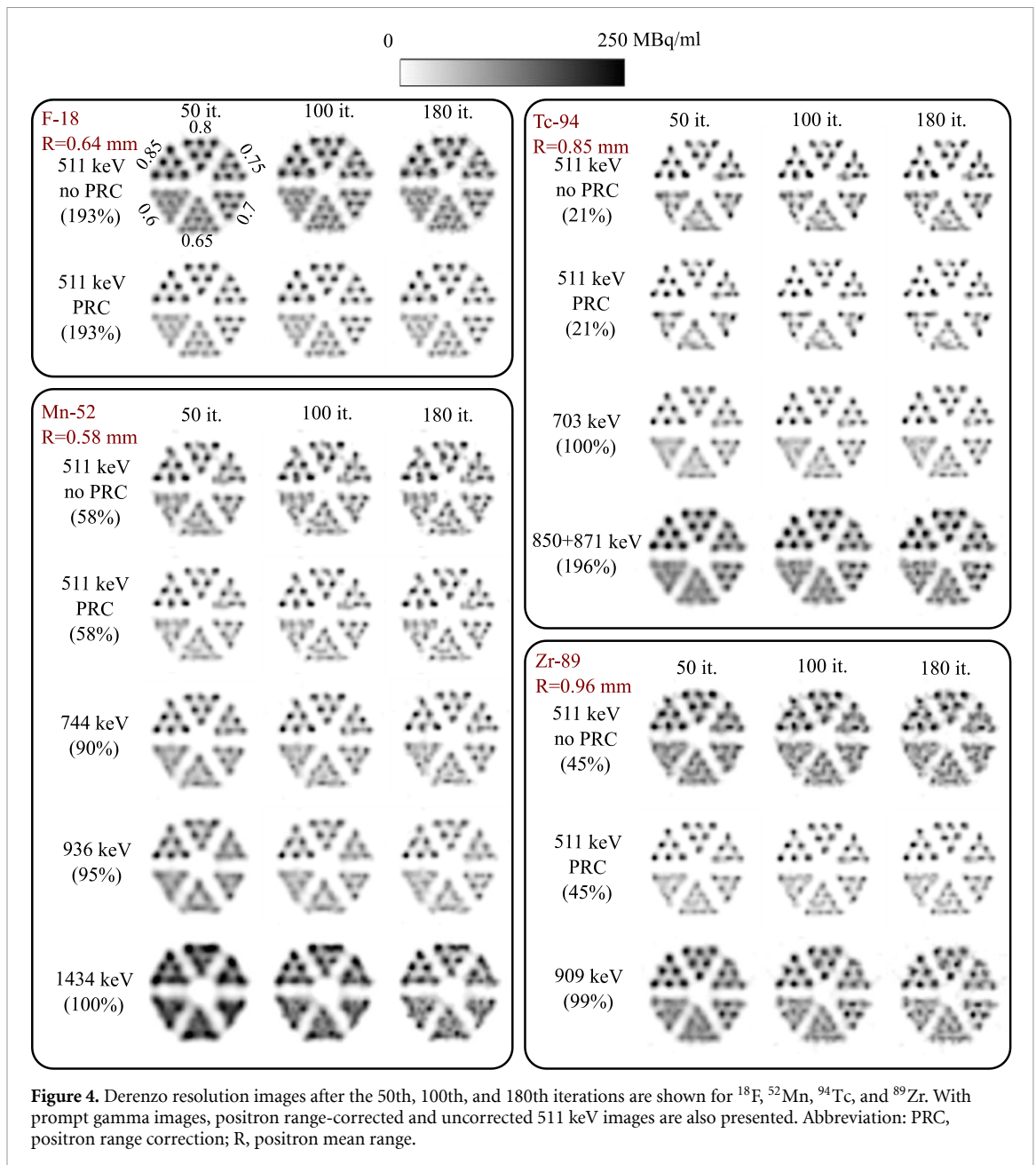
1.2 MeV and 1.4 MeV from ⁴⁴Sc and ⁵²Mn isotopes yield resolutions of ~ 0.75 mm and ~ 0.8 mm, respectively. As expected, image resolution generally degrades with increasing gamma energy. On the contrary, the resolution achieved for ⁴⁴Sc using the 1.2 MeV prompt emission is superior to that obtained with the 1.0 MeV gamma emission from ⁶⁶Ga. This is likely due to significant collimator and detector down scatter from higher energy gammas of 2.2 MeV and 2.8 MeV emitted by ⁶⁶Ga (figure 3) contributing to the photopeak of low intensity (37% in table 1).

PRC enhanced the image quality of 511 keV reconstructed images across all isotopes. Note that the PRC applied in this study was conducted under ideal conditions as positron range in an infinite water medium was used which corresponds well to that in the phantom simulations, given the similar attenuation characteristics of water and PMMA, the two materials used in the digital phantom definition. In contrast, PRC in small animal scans is a nontrivial task due to the presence of different types of tissues within a relatively complex three-dimensional distribution (Cal-Gonzalez *et al* 2015). Nonetheless, for all isotopes, prompt emissions, which do not suffer from positron range, produced images of better resolutions than the 511 keV with PRC, except for ⁴⁴Sc. The maximum achievable resolutions for the examined isotopes are listed in table 4. For 2.2 MeV prompt gamma emission of ³⁸K, PSFs were too broad to resolve the largest diameter rods (0.85 mm). Images obtained from a second Derenzo resolution phantom containing larger rod diameters demonstrate a supra-mm resolution of 1.2 mm when using 2.2 MeV gamma radiation from this isotope (see figure A1 in appendix A.2).

3.5. Uniformity studies

Uniformity phantom images reconstructed using both 511 keV and the available prompt gamma emissions for all isotopes under study are presented in figures 6 and 7. The images correspond to the 50th iteration and include both positron range-uncorrected and corrected 511 keV images. Additional uniformity phantom images at the 100th iteration are provided in the supplementary material (figures S2 and S3). The percentage uniformity (equation (1)) is plotted against the iteration number for each isotope in figure 8.

The granular-like texture visible in the uniformity images arises from statistical noise inherent in the projection data combined with the used post-filter (1 mm). This is illustrated in figure S5, where we show that as the FWHM of the Gaussian filter increases, the noise spikes progressively transform into a granular texture. Besides, the transaxial views of the 511 keV images of ⁵²Mn, ⁹⁴Tc, and ⁸⁶Y reveal a pattern consisting of three lines of dots intersecting at equal angles, slightly offset from the center of the cylindrical phantom while the coronal views of the same three isotopes exhibit a parallel, tubular-like arrangement of dots along the axis of the phantom, rather than a uniform distribution. We used GATE's 'ComptonPhantom' and 'ComptonCrystal' flags to reject collimator and detector down scatter from projection data respectively and we found that the artifact in the transaxial view is due to the detector down scatter contribution from high

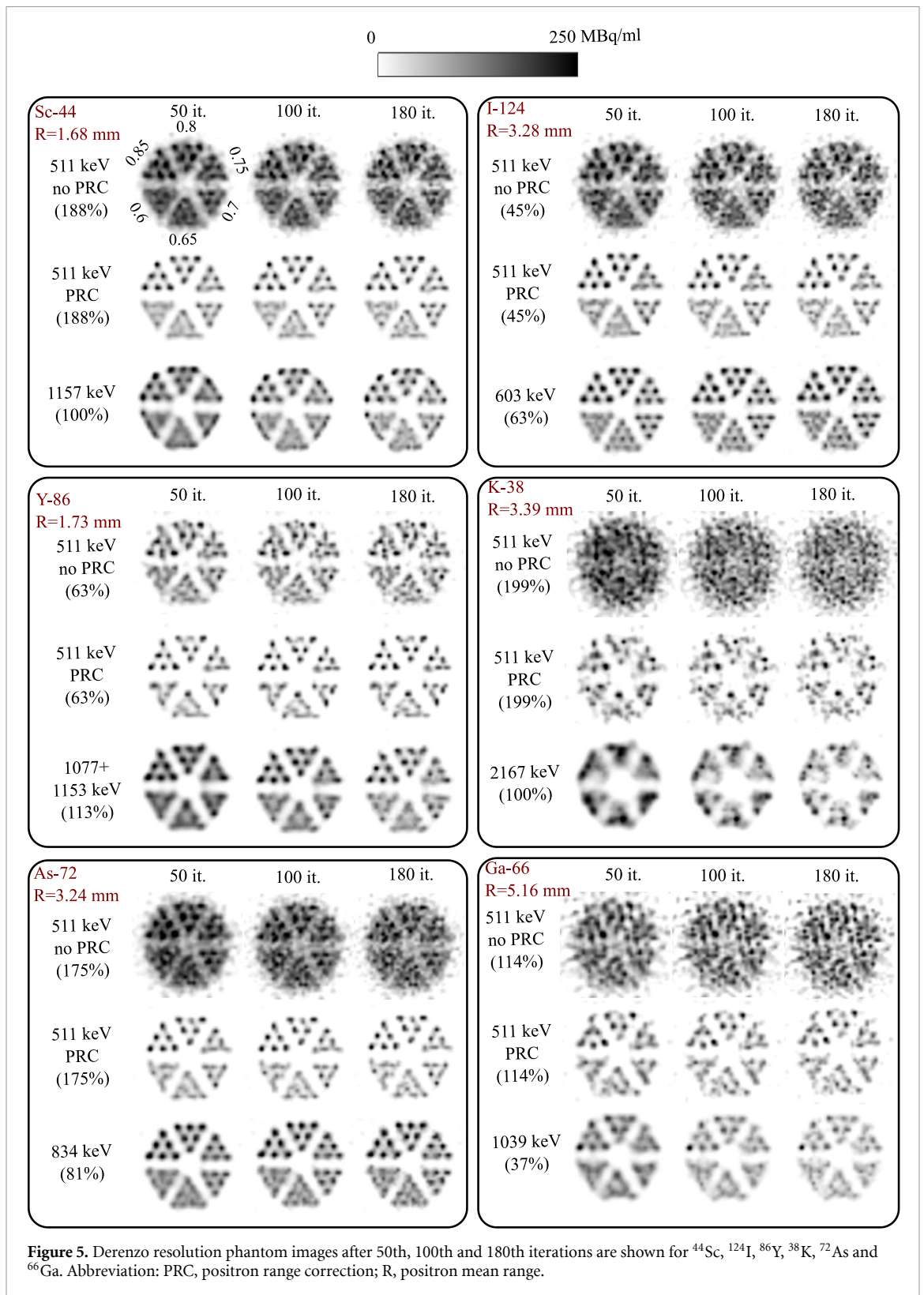


and ultra-high energy prompt gammas (figure S6). The artifact in the coronal view, however, could not be attributed specifically to detector or collimator down scatter (figure S6); it appeared when both types of down scatter were present in the projection data.

3.6. Ultra-high energy imaging

The 1.4 MeV prompt gamma emissions of ^{52}Mn are reconstructed using forward matrices with 1%, 3%, 5%, and 7% cutoffs and images are displayed in figure 9. Images with 1% cutoff exhibit ring artifacts (Li and Koral 2007), characterized by a visible dip at the center of phantoms due to enhanced edges. Such ring artifacts have been observed in PSF-based PET reconstruction also, when PSFs are broad (Tong *et al* 2011, Rahmim *et al* 2013). In fact, in the 1.2 MeV image of ^{44}Sc (figure 5), a slight ring artifact is also noticeable, but it becomes distinctively recognizable at 1.4 MeV. Conversely, at 2.2 MeV, no rods were visible (figure 5), and therefore, we did not perform a similar analysis.

These ring artifacts cannot be eliminated even with a large number of iterations (1000 it. in figure 9) for a 1% cutoff. It can however be mitigated by using higher cutoffs in matrix generation (*e.g.* 3%, 5%, 7%), as using higher cutoffs effectively sharpens the PSFs by truncating the tails. Also, resolution phantom images reconstructed using the 1% cutoff matrix exhibit rounding at the outer edges, resulting in a reduction in the size of the phantom compared to its original dimension. Line profiles through six hot rods further support this observation (figure 10). A similar artifact of size reduction was observed in the uniformity phantom



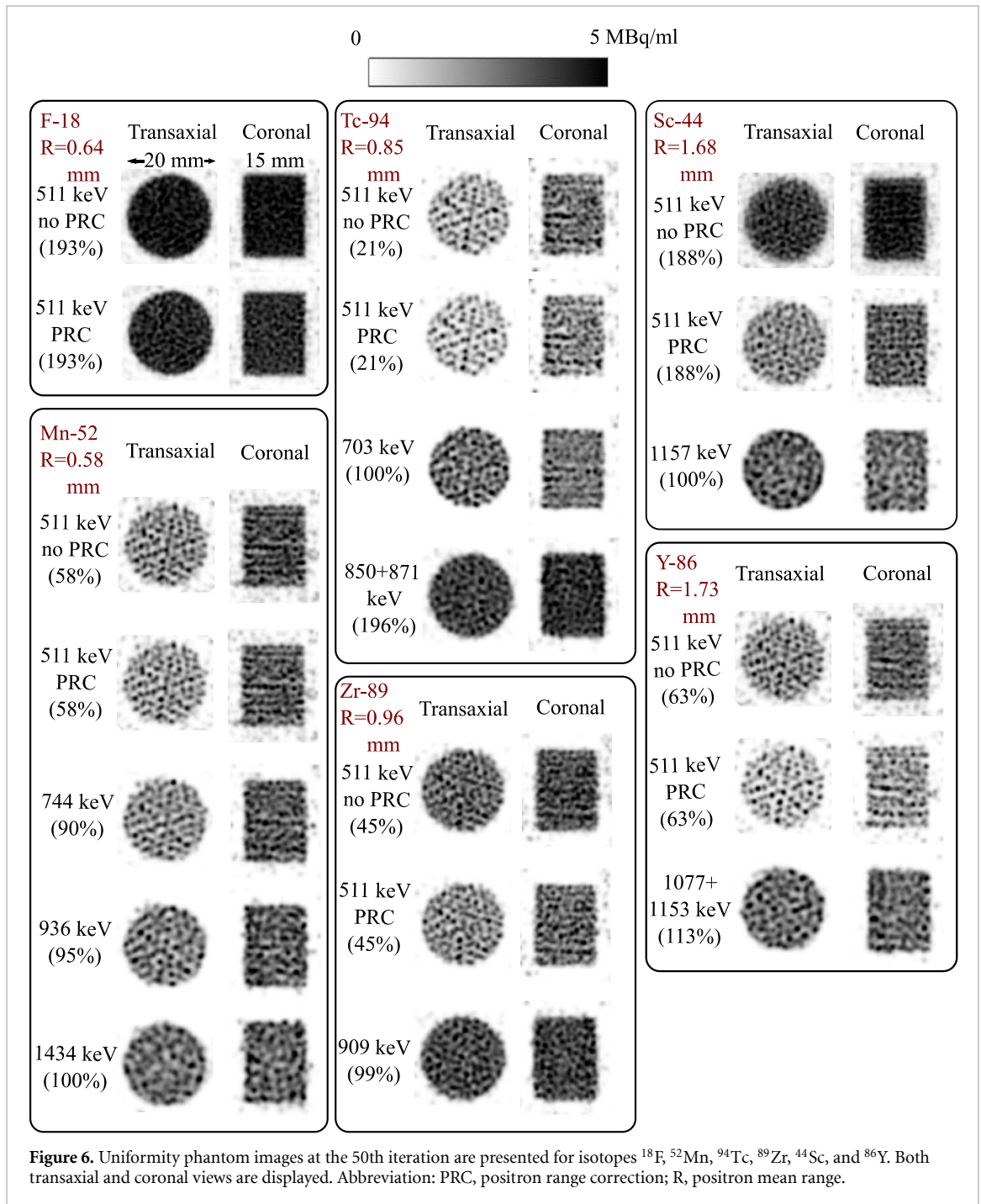
images at ultra-high energies (appendix A.3). This effect may be attributed to the inability of broad PSFs to reconstruct high-frequency information at the periphery. The use of higher cutoffs allows for a more realistic reconstruction of the phantom's outer edges.

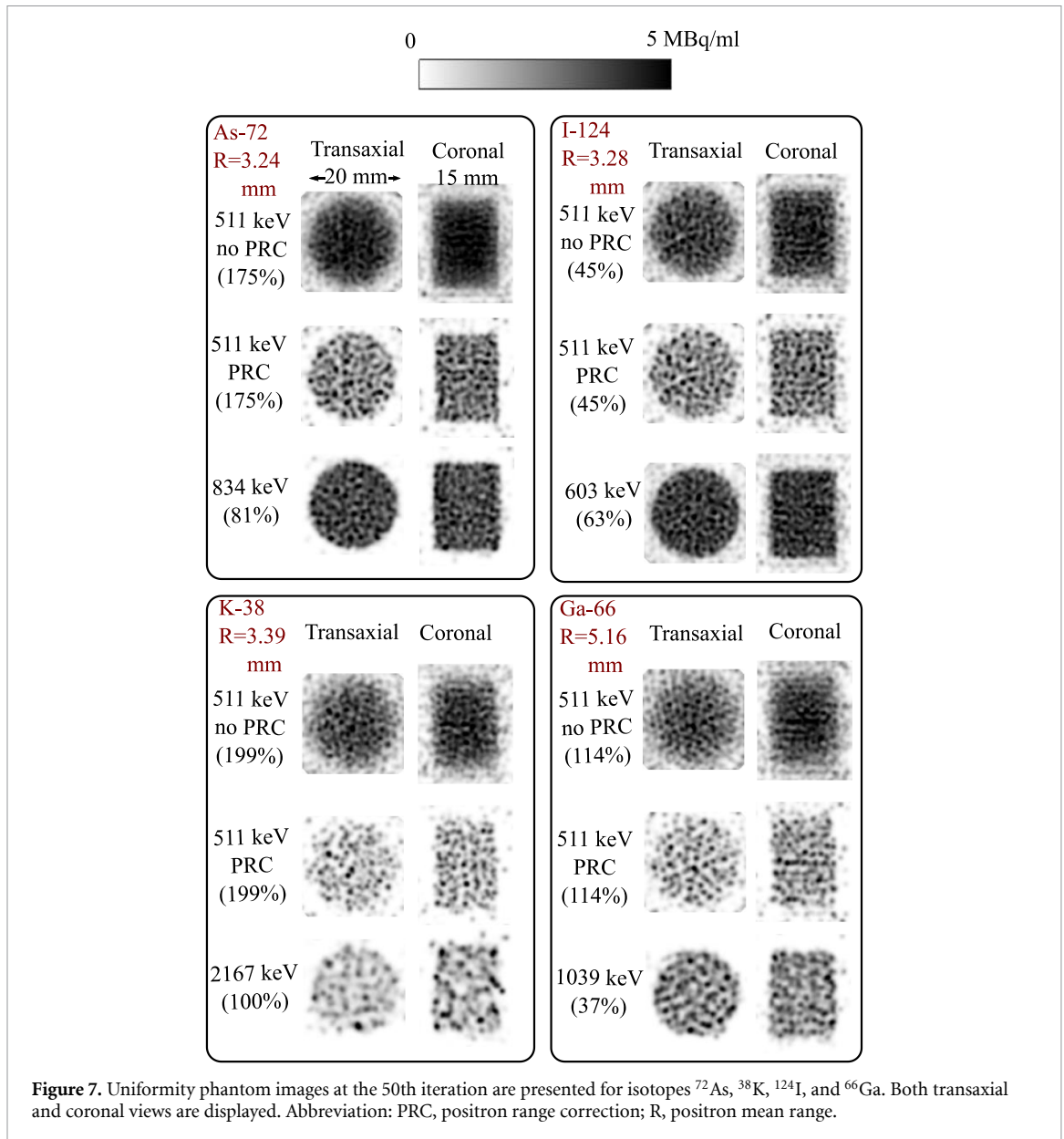
4. Discussion

In this study, we assessed the resolutions that can be obtained for challenging PET isotopes when imaged with a high energy multi-pinhole scanner. Achieving a high resolution for these isotopes using conventional

Table 4. Highest achievable resolutions for nine isotopes under study.

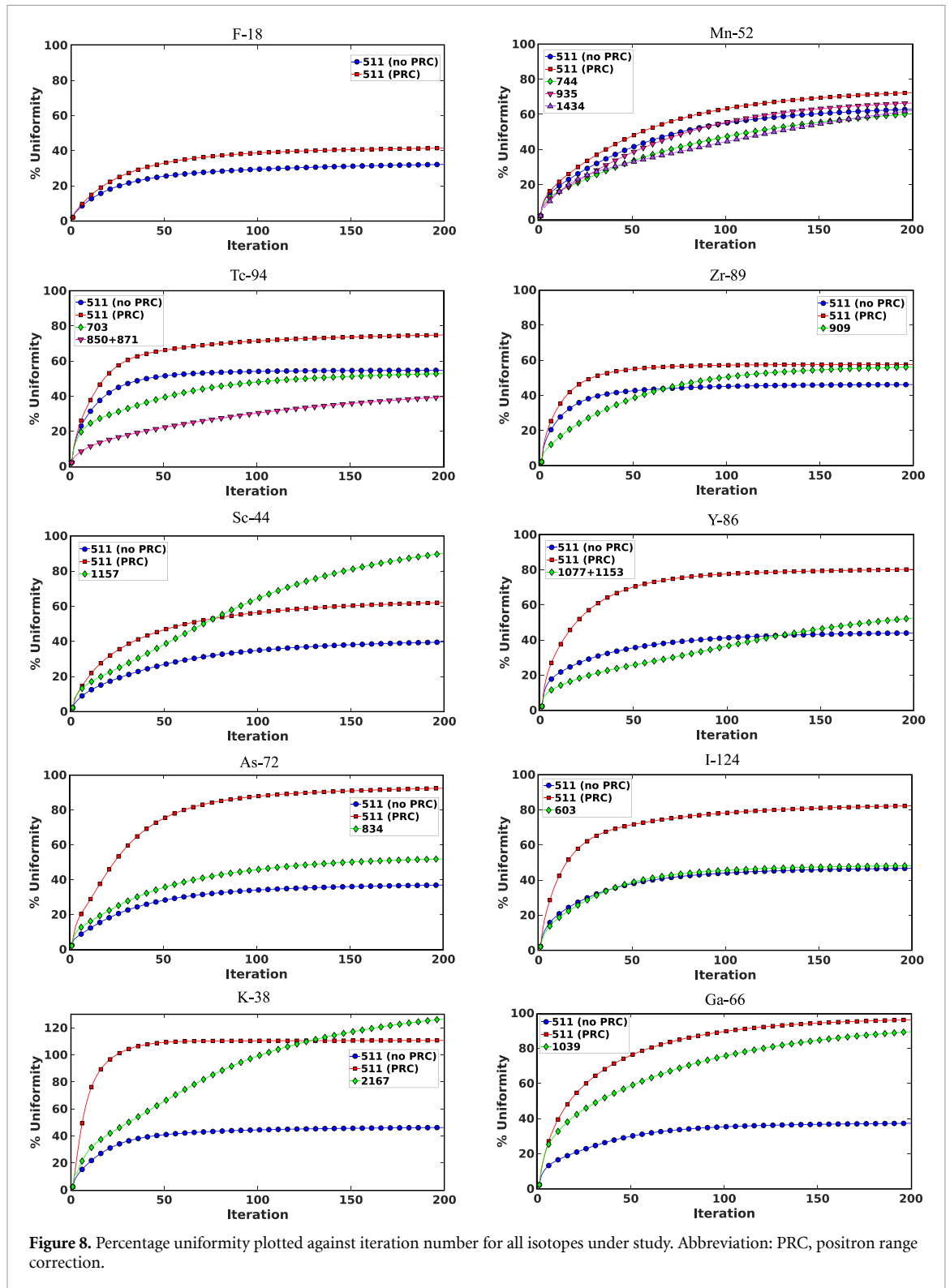
Isotope	Gamma used	Resolution (mm)
⁵² Mn	744 keV	0.7
⁹⁴ Tc	703 keV	0.7
⁸⁹ Zr	909 keV	0.7
⁴⁴ Sc	511 keV	0.7
⁸⁶ Y	1077 + 1153 keV	0.75
⁷² As	834 keV	0.7
¹²⁴ I	603 keV	0.65
³⁸ K	2167 keV	1.2
⁶⁶ Ga	1039 keV	0.8



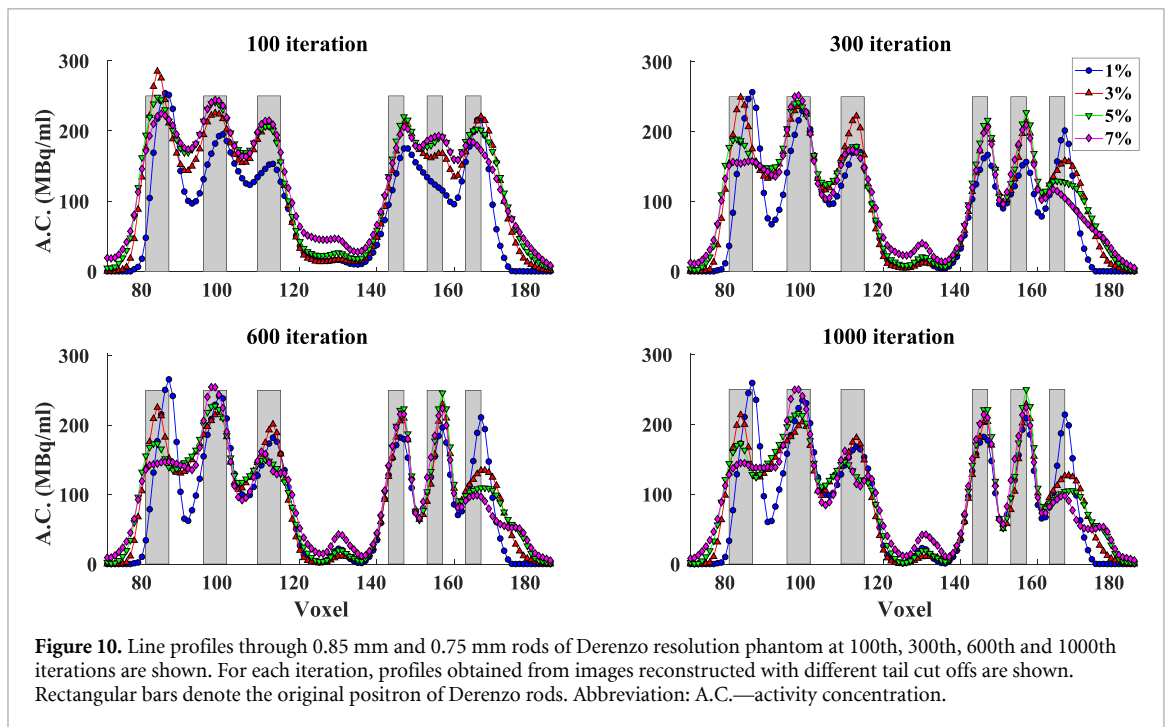
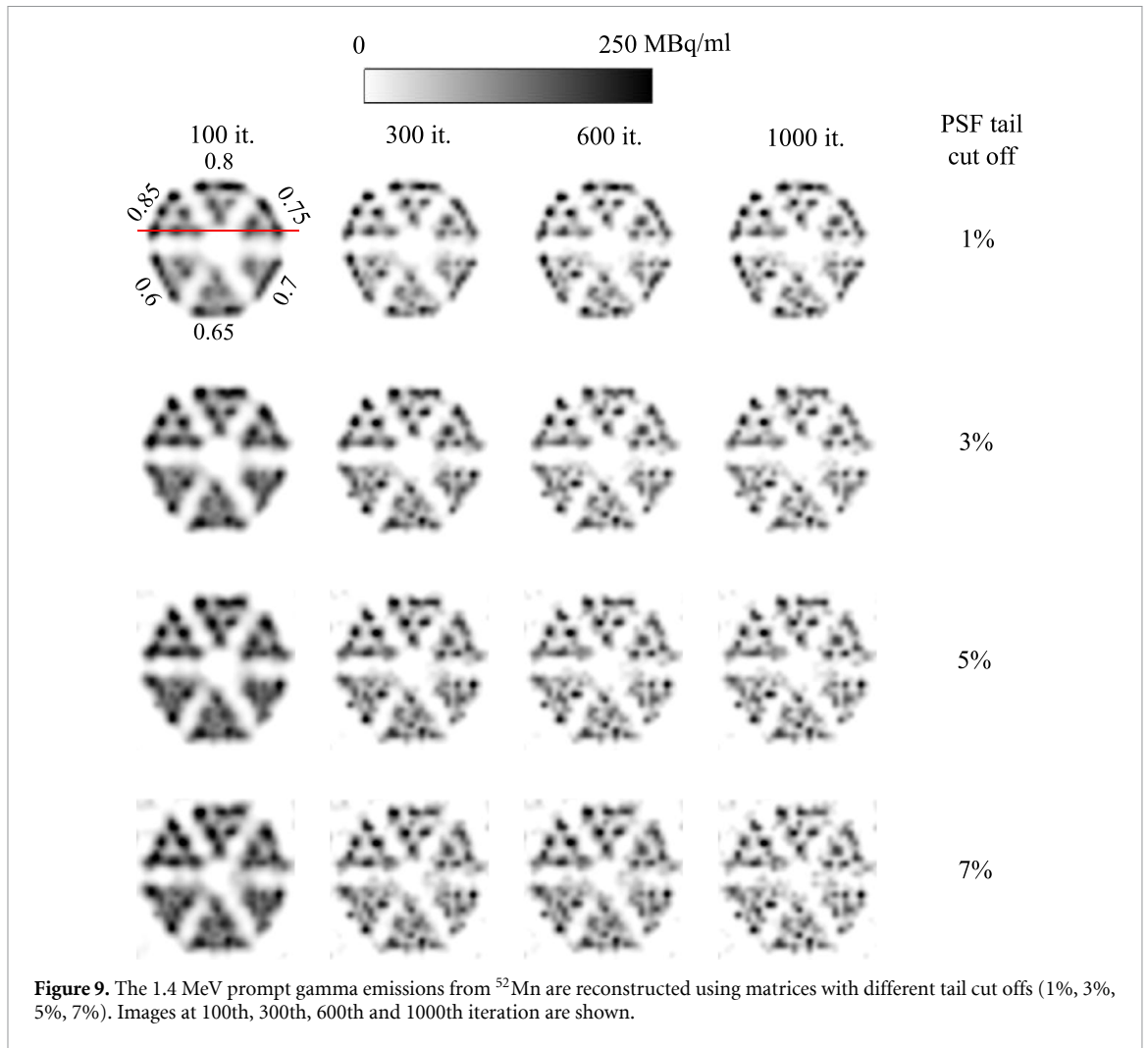


coincidence preclinical PET is challenging due to their long positron ranges or the down scatter of the prompt gammas into the 511 keV photopeak (Laforest *et al* 2002). To circumvent these issues, VECTor utilizes prompt gamma emissions to image these isotopes instead of the 511 keV annihilation photons (Beekman *et al* 2021). The resolutions obtained for the tested isotopes were in the sub-millimeter range (table 4), except for ^{38}K , for which 1.2 mm resolution can be realized by using the 2.2 MeV prompt emission (figure A1 in appendix A.2). To the best of our knowledge, this capability is unique to PET with cluster pinhole collimation.

In this simulation, we modeled the VECTor system with a thin scintillator crystal (9.5 mm). This choice was motivated by the imaging study in (Beekman *et al* 2021), where ^{124}I and ^{89}Zr were imaged using a VECTor scanner with a 9.5 mm crystal, providing us with experimental data to see how well they match our simulations. A thicker crystal, such as the 19 mm XT crystal offered by MILabs, may prove advantageous for imaging low-intensity ultra-high energy gamma emissions, such as the 1039 keV (37%) gamma of ^{66}Ga . The 19 mm crystal demonstrates a sensitivity approximately 2.8 times greater than the 9.5 mm crystal at this energy. However, an effective depth-of-interaction (DOI) correction algorithm will be required to optimize performance (Cosmi *et al* 2024b). Notably, the resolutions achieved in this work for ^{124}I and ^{89}Zr were 0.65 mm and 0.7 mm, respectively. In the previous experimental study (Beekman *et al* 2021), 0.75 mm rods of ^{124}I could be distinguished in the resolution phantom. However, since the phantom used did not contain smaller 0.65 mm or 0.7 mm rods, a direct comparison of image resolution is not possible. For ^{89}Zr the experiments indicated a 0.75 mm image resolution which is close to the 0.7 mm resolution reported in this



work. The small difference may be explained by the higher activity concentration used in the simulation, the limited ability to include all image degrading effects of the detector in the simulation and perfect modeling of the system matrix that is not possible in an experimental situation. Overall, this work specifically demonstrates that the cluster collimation technology (Beekman 2011) used in the VECTor scanner can achieve sub-millimeter resolution even at ultra-high energies, as high as 1.4 MeV. Based on our results, we attribute the degradation of images at very high energies primarily to the following factors: (i) pinhole edge and collimator wall penetration, and (ii) down scatter from higher energy emissions within the photopeak, which is isotope-dependent.



In this simulation study, we modeled the detector response by assuming a simple Gaussian model for the energy-dependent energy resolution instead of detailed simulations of the scintillator light transport or electronics. This is certainly an over-simplification for ultra-high energies. Currently, the VECTor scanner detector electronics is optimized for energies up to 1.2 MeV and it would need to be upgraded to a wider energy range to perform imaging studies at higher energies. Upgrading the detector for a wide energy range, e.g. from 20 keV to 2.3 MeV, presents several technical challenges (Villena *et al* 2010). Non-linearity in PMT response and electronics can affect energy calibration, while maintaining uniformity across the field of view becomes increasingly difficult due to varying detection efficiencies at different energies. Additionally, count rate performance may degrade at higher energies due to pulse pile-up and extended dead time in the electronics. Thus, while we validated the current collimator for the investigated isotopes, the suitability of the detector in real experiments was not yet verified for energies >1.2 MeV.

Ring artifacts were observed in ultra-high energy images (figure 9). We found that using a higher cutoff forward matrix could mitigate these ring artifacts. This might seem contradictory to previous findings (Goorden *et al* 2016), where a lower cutoff of 1% (as opposed to 20% used in 140 keV imaging) improved image resolution and uniformity at 511 keV. This contradiction can be explained by considering that, in the VECTor system, at ultra-high energies, PSFs become broad due to enhanced edge penetration and significant wall penetration (figure 2), rendering the reconstruction problem underdetermined and leading to ring artifacts. Wall penetration can be mitigated by using a thicker collimator or an additional independent outer casing on top of the collimator. However, edge penetration cannot be reduced in this manner, which is the primary reason for the gradual degradation of image resolution with increasing energy (figures 4 and 5). This effect can be reduced by reducing the opening angle of the pinholes, but that requires sophisticated cluster geometries to maintain FOV (e.g. twisted cluster pinholes Cosmi *et al* 2024a or superclusters Beekman 2022, Phuong Nguyen *et al* 2022). Furthermore, additional artifacts were present in the 511 keV uniformity images of isotopes exhibiting pronounced down scatter (^{52}Mn , ^{94}Tc and ^{86}Y) due to higher energy prompts. Our analysis revealed that these artifacts arise either due to detector down scatter (transaxial view) or a combination of detector and collimator scatter (coronal view). Hence, implementing a scatter correction scheme which goes beyond the used triple energy window method similar to (Ouyang *et al* 2007) may improve imaging performance for these challenging isotopes.

Many of the isotopes studied have more than one prompt gamma with sufficient intensity, such as ^{52}Mn , ^{94}Tc , and ^{86}Y . In subsequent studies, we will perform a feasibility study of the joint reconstruction of multiple prompt gamma energies simultaneously. This approach may enable achieving comparable image quality with reduced activity levels and/or shorter acquisition times, which is particularly relevant for dose quantification in alpha-particle radiotherapies. Additionally, for isotopes like ^{89}Zr , ^{52}Mn , and ^{94}Tc , which have relatively short positron ranges, it may be worthwhile to investigate joint reconstruction with the 511 keV annihilation photons. Lastly, the current design of the cluster multi-pinhole collimator is prone to ring artifacts at ultra-high energies specifically from 1.2 MeV. Therefore, developing a mitigation technique to eliminate these artifacts will be a priority in the future.

5. Conclusion

Our research indicates that cluster pinhole collimators are suitable for sub-millimeter resolution for 9 out of the 10 PET isotopes studied in this paper, including those with long positron ranges by utilizing prompt emissions of high intensity at one or multiple energies. For example impressive ~ 0.8 mm image resolutions at gamma energies as high as 1.4 MeV were attained. The unique capability of cluster pinhole collimation to enable sub-mm resolution for such a diverse set of challenging isotopes can enable a wide range of applications in development of new tracers and therapies.

Data availability statement

All data that support the findings of this study are included within the article (and any supplementary information files).

Acknowledgments

This work was supported by the research Grant QUARAT: Quantitative Universal Radiotracer Tomography (TTW16885), which is partially funded by the Dutch Research Council (NWO). The authors wish to express their gratitude to Dr Chris Kamphuis of MILabs B V, The Netherlands, for providing information on the detector energy resolutions of VECTor scanner at various energies.

Appendix

A.1. Positron range

We conducted a comparative analysis of positron range distributions obtained from GATEv9.0 against another software called PeneloPET (Cal-González *et al* 2013), a track structure code developed by Le Loirec and Champion (2007a, 2007b, 2007c) and semi-empirical formula by Evans and Evans (1955). Most of the literature studied a particular one dimensional distribution:

$$\text{aPSF}_{\text{sin}} = \int_{-\infty}^{\infty} dz \int_{-\infty}^{\infty} \text{aPSF}(x, y, z) dy. \quad (\text{A1})$$

where aPSF (annihilation PSF) is three dimensional distribution of annihilation points. Derenzo (1986) showed that aPSF_{sin} can be modeled by double exponential function:

$$P(x) = Ce^{-k_1x} + (1 - C)e^{-k_2x}. \quad (\text{A2})$$

We compared the fitting parameters (C, k_1, k_2) obtained from GATE data with those reported by Cal-Gonzalez *et al* (2013) and Loirec *et al* (2007a, 2007b, 2007c) (table A1), maintaining a consistent bin size of 10 micrometers. Additionally, we compared the mean positron range obtained from GATE with (Le Loirec and Champion 2007a, 2007b, 2007c, Cal-González *et al* 2013) (table A2). The mean ranges reported by Cal-Gonzalez *et al* (2013) and Loirec *et al* (2007a, 2007b, 2007c) were derived from two-dimensional projection distributions of the original three-dimensional distribution of annihilation points. Accordingly, we projected the original three-dimensional annihilation distribution obtained from GATE onto a two-dimensional plane to calculate the mean ranges. Evans and Evans (1955) estimated the mean range using a semi-empirical expression

$$R_{\text{mean}}(\text{cm}) = \frac{0.108 [E_{\beta}^{\text{max}}(\text{MeV})]^{1.14}}{\rho(\text{gm cm}^{-3})}. \quad (\text{A3})$$

Positron range values reported in the literature exhibit considerable variation. Upon reaching thermal velocity, a positron will either annihilate directly with an electron or form a hydrogen like positronium atom. Due to its neutral charge, positronium does not interact electromagnetically, allowing it to drift depending on its residual momentum and half life. The formation probability of positronium is influenced by the energy of the beta particle and the medium.

Most Monte Carlo codes, such as GATE, PeneloPET, and EGSnrc, utilize cross-sections from Heitler (1954), which do not account for positronium formation. To the best of our knowledge, Le Loirec and Champion (2007a, 2007b, 2007c) have incorporated positronium formation in their track structure code. This may explain why the positron ranges reported by them are systematically larger compared to those from GATE, PeneloPET (Cal-González *et al* 2013), and the semi-empirical formula by Evans and Evans (1955) (table A2). However, it is noteworthy that the positronium yield in water reported by Champion and Le Loirec (2007) (83%) significantly deviates from the values reported in other sources, such as Castellaz *et al* (2002), Colombino *et al* (1965), and Abuelhia *et al* (2007), which are approximately 30%.

Table A1. Comparing fitting parameters of equation (A2) obtained from analysing GATE (v9.0) data with PeneloPET (Cal-González *et al* 2013) and Loirec *et al* (2007a, 2007b, 2007c). Only k_2 values were given for PeneloPET (Cal-González *et al* 2013).

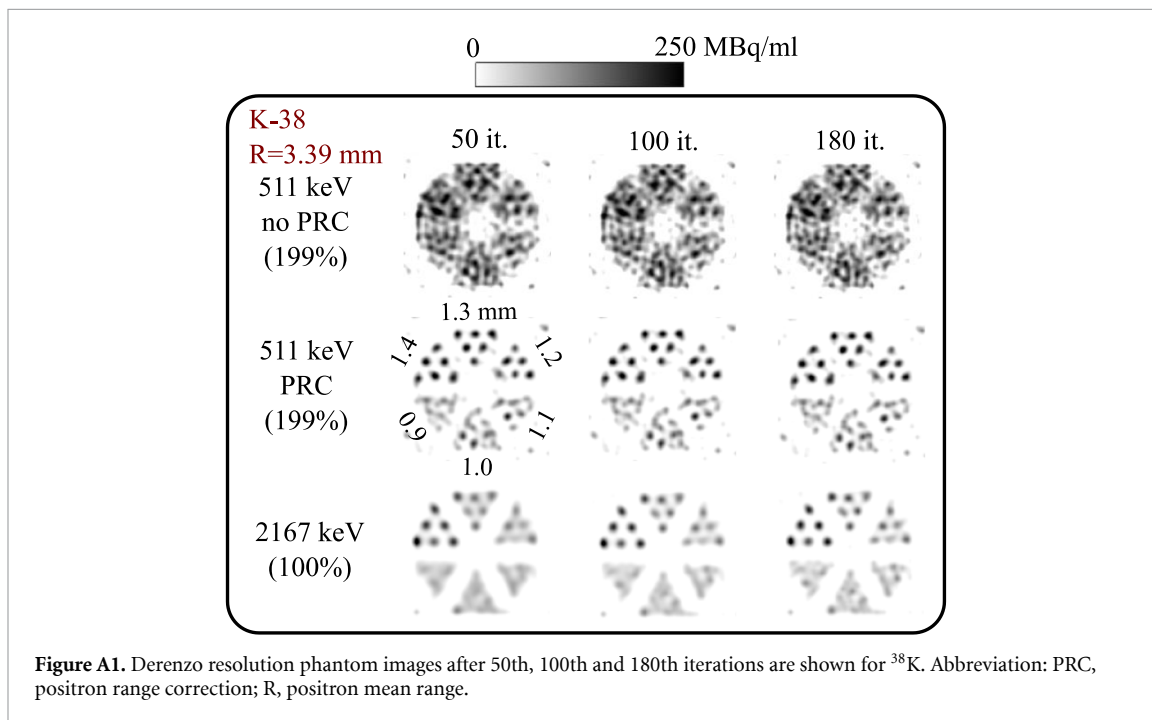
	C	C	k_1 (mm ⁻¹)	k_1 (mm ⁻¹)	k_2 (mm ⁻¹)	k_2 (mm ⁻¹)	k_2 (mm ⁻¹)
Isotope	GATE (v9.0)	Le Loirec and Champion (2007a, 2007b, 2007c)	GATE (v9.0)	Le Loirec and Champion (2007a, 2007b, 2007c)	GATE (v9.0)	PeneloPET (Cal-González <i>et al</i> 2013)	Le Loirec and Champion (2007a, 2007b, 2007c)
¹⁸ F	0.68	—	76.48	—	4.81	3.27	—
¹¹ C	0.66	0.61	58.95	30.91	2.46	1.79	1.49
¹³ N	0.65	0.58	53.45	22.12	1.75	1.3	1.07
¹⁵ O	0.63	0.56	41.37	16.84	0.98	0.77	0.6
⁶⁸ Ga	0.71	0.34	50.54	13.81	0.94	0.67	0.49
⁸² Rb	0.65	—	36.59	—	0.41	0.31	—
⁵² Mn	0.73	0.39	97.69	19.92	6.13	6.13	2.79
⁸⁹ Zr	0.75	0.29	79.84	17.68	3.22	—	1.42
⁴⁴ Sc	0.69	0.33	53.76	10.74	1.34	—	0.71
⁸⁶ Y	0.77	0.4	64.41	7.89	1.70	—	0.76
⁷² As	0.70	0.5	41.47	14.82	0.60	—	0.35
¹²⁴ I	0.77	0.39	57.27	8.38	1.18	—	0.54
³⁸ K	0.39	0.38	10.27	11.7	0.48	—	0.3
⁶⁶ Ga	0.83	0.79	41.48	7.46	0.35	—	0.2

Table A2. Positron mean range compared between GATE (v9.0), PeneloPET (Cal-González *et al* 2013), Monte Carlo track structure code by Le Loirec and Champion (2007a, 2007b, 2007c) and semi-empirical formula by Evans and Evans (1955) for PET isotopes under study and other.

	R_{mean} (mm)	R_{mean} (mm)	R_{mean} (mm)	R_{mean} (mm)
Isotope	GATE (v9.0)	PeneloPET (Cal-González <i>et al</i> 2013)	Le Loirec and Champion (2007a, 2007b, 2007c)	Evans and Evans (1955)
¹⁸ F	0.38	0.57	0.66	0.64
¹¹ C	0.77	1.02	1.27	1.03
¹³ N	1.08	1.40	1.73	1.33
¹⁵ O	1.88	2.34	2.97	2.02
⁶⁸ Ga	2.03	2.69	3.56	2.23
⁸² Rb	4.37	5.33	7.49	4.18
⁵² Mn	0.67	—	0.63	0.58
⁸⁹ Zr	0.63	—	1.27	0.96
⁴⁴ Sc	1.44	—	2.46	1.68
⁸⁶ Y	2.52	—	2.51	1.73
⁷² As	3.31	—	5.19	3.24
¹²⁴ I	2.22	—	3.37	3.28
³⁸ K	4.48	—	5.67	3.39
⁶⁶ Ga	7.49	—	8.69	5.16

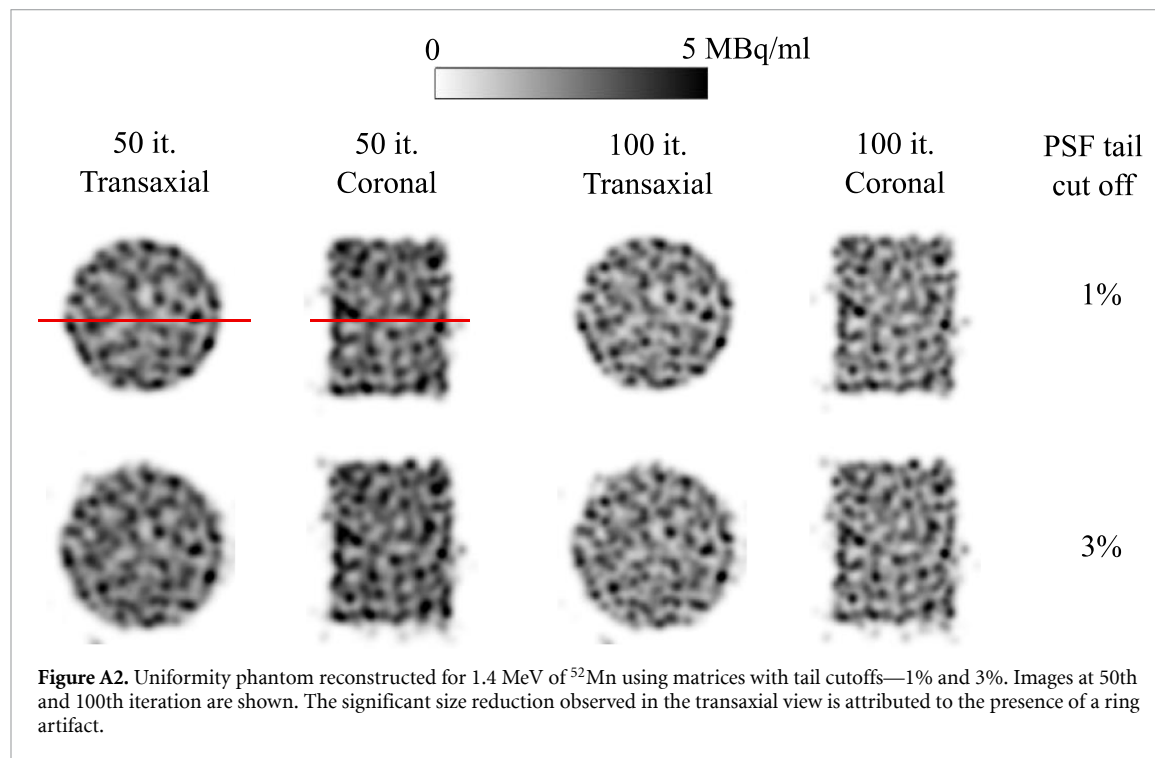
A.2. Determining resolution for ^{38}K

Figure A1 presents the ^{38}K reconstructed images for the second Derenzo resolution phantom with larger diameter rods. Following the convention outlined in section 2.3, a 5% cutoff matrix was employed to reconstruct the 2167 keV gamma to avoid the ring artifact. Both the 511 keV gamma, with PRC, and the 2167 keV gamma are capable of resolving the 1.2 mm rods, with the 2167 keV reconstruction exhibiting lower noise compared to the 511 keV.



A.3. Ring artifact in uniformity phantom

At the ultra-high energy of 1.4 MeV for ^{52}Mn , a size reduction artifact appears in the transaxial view of the reconstructed uniformity phantom images when a 1% cutoff matrix is used (figure A2). Similar to the resolution phantom case, a slightly larger cutoff matrix was employed to mitigate this artifact. Line profiles shown in figure S4 in supplementary material confirm that using a higher cutoff matrix can effectively reduce the artifact.



ORCID iDs

Satyajit Ghosh  <https://orcid.org/0000-0001-6334-1185>

Valerio Cosmi  <https://orcid.org/0009-0008-2748-2202>

Marlies C Goorden  <https://orcid.org/0009-0007-2202-5371>

References

- Abuelhia E, Kacperski K and Spyrou N M 2007 Three-photon annihilation in PET: 2D imaging experiments *J. Radioanal. Nucl. Chem.* **271** 489–95
- Agostinelli S *et al* 2003 Geant4—a simulation toolkit *Nucl. Instrum. Methods Phys. Res. A* **506** 250–303
- Anizan N, Carlier T, Hindorf C, Barbet J and Bardiès M 2012 Acquisition setting optimization and quantitative imaging for 124I studies with the Inveon microPET-CT system *EJNMMI Res.* **2** 7
- Barrett H H and Swindell W 1981 *Radiological Imaging—The Theory of Image Formation, Detection, and Processing* (Academic Press)
- Beekman F J 2011 Focused pinhole gamma detection device *US Patent* 8067741B2
- Beekman F J 2022 SPECT-scanner and collimator *US Patent* 11937956B2
- Beekman F J, Kamphuis C, Koustoulidou S, Ramakers R M and Goorden M C 2021 Positron range-free and multi-isotope tomography of positron emitters *Phys. Med. Biol.* **66** 065011
- Branderhorst W, Vastenhouw B and Beekman F J 2010 Pixel-based subsets for rapid multi-pinhole SPECT reconstruction *Phys. Med. Biol.* **55** 2023–34
- Cal-González J, Herraiz J L, España S, Corzo P M G, Vaquero J J, Desco M and Udias J M 2013 Positron range estimations with PeneloPET *Phys. Med. Biol.* **58** 5127–52
- Cal-Gonzalez J, Perez-Liva M, Herraiz J L, Vaquero J J, Desco M and Udias J M 2015 Tissue-dependent and spatially-variant positron range correction in 3D PET *IEEE Trans. Med. Imaging* **34** 2394–403
- Castellaz P, Siegle A and Stoll H 2002 Positron age-momentum-correlation (AMOC) measurements on organic liquids *J. Nucl. Radiochem. Sci.* **3** R1–7
- Champion C and Le Loirec C 2007 Positron follow-up in liquid water: II. Spatial and energetic study for the most important radioisotopes used in PET *Phys. Med. Biol.* **52** 6605–25
- Cho Z, Chan J K, Erickson L, Singh M, Graham S, MacDonald N S and Yano Y 1975 Positron ranges obtained from biomedically important positron-emitting radionuclides *J. Nucl. Med.* **16** 1174–6
- Chris Kamphuis D 2024 personal communication

- Colombino P, Fiscella B and Trossi L 1965 Study of positronium in water and ice from 22 to $-144\text{ }^{\circ}\text{C}$ by annihilation quanta measurements *Il Nuovo Cim.* **38** 707–23
- Conti M and Eriksson L 2016 Physics of pure and non-pure positron emitters for PET: a review and a discussion *EJNMMI Phys.* **3** 8
- Cosmi V, Kvassheim M, Ghosh S, Beekman F J and Goorden M C 2024a Twisted clustered pinhole collimation for improved high-energy preclinical SPECT/PET *Phys. Med. Biol.* **69** 225016
- Cosmi V, Wang B, Goorden M C and Beekman F J 2024b NaI gamma camera performance for high energies: effects of crystal thickness, photomultiplier tube geometry and light guide thickness *Med. Phys.* **51** 4696–708
- Crişan G, Moldovean-Cioroianu N S, Timaru D-G, Andrieş G, Căinap C and Chiş V 2022 Radiopharmaceuticals for PET and SPECT imaging: a literature review over the last decade *Int. J. Mol. Sci.* **23** 5023
- Derenzo S E 1986 Mathematical removal of positron range blurring in high resolution tomography *IEEE Trans. Nucl. Sci.* **33** 565–9
- Derenzo S 1979 Precision measurement of annihilation point spread distributions for medically important positron emitters *5th Int. Conf. in Positron Annihilation (Lake Yamanaka, Japan)*
- Duboc D, Kahan A, Maziere B, Loc'H C, Crouzel C, Menkès C J, Amor B, Strauch G, Guérin F and Syrota A 1991 The effect of nifedipine on myocardial perfusion and metabolism in systemic sclerosis. A positron emission tomographic study *Arthritis Rheum.* **34** 198–203
- Eppard E, de la Fuente A, Benešová M, Khawar A, Bundschuh R A, Gärtner F C, Kreppel B, Kopka K, Essler M and Rösch F 2017 Clinical translation and first in-human use of [44Sc]Sc-PSMA-617 for PET imaging of metastasized castrate-resistant prostate cancer *Theranostics* **7** 4359–69
- Evans R D and Evans R D 1955 *The Atomic Nucleus* vol 582 (McGraw-Hill)
- Glaudemans A W J M, de Vries E F J, Galli F, Dierckx R A J O, Slart R H J A and Signore A 2013 The use of 18F-FDG-PET/CT for diagnosis and treatment monitoring of inflammatory and infectious diseases *Clin. Dev. Immunol.* **2013** 1–14
- Goorden M C, Kamphuis C, Ramakers R M and Beekman F J 2020 Accelerated image reconstruction by a combined dual-matrix dual-voxel approach *Phys. Med. Biol.* **65** 105014
- Goorden M C, van der Have F, Kreuger R and Beekman F J 2011 An efficient simulator for pinhole imaging of PET isotopes *Phys. Med. Biol.* **56** 1617–34
- Goorden M C, van der Have F, Kreuger R, Ramakers R M, Vastenhout B, Burbach J P H, Booi J, Molthoff C F M and Beekman F J 2013 VECTor: a preclinical imaging system for simultaneous submillimeter SPECT and PET *J. Nucl. Med.* **54** 306–12
- Goorden M C, van Roosmalen J, van der Have F and Beekman F J 2016 Optimizing modelling in iterative image reconstruction for preclinical pinhole PET *Phys. Med. Biol.* **61** 3712–33
- Graves S A et al 2015 Novel preparation methods of 52Mn for ImmunoPET imaging *Bioconjug. Chem.* **26** 2118–24
- Heitler W 1954 *The Quantum Theory of Radiation* 3rd edn (Dover Publications, Inc.)
- Jan S et al 2004 GATE: a simulation toolkit for PET and SPECT *Phys. Med. Biol.* **49** 4543–61
- Jennewein M et al 2008 Vascular imaging of solid tumors in rats with a radioactive arsenic-labeled antibody that binds exposed phosphatidylserine *Clin. Cancer Res.* **14** 1377–85
- Jentzen W, Freudenberg L, Eising E G, Sonnenschein W, Knust J and Bockisch A 2008 Optimized 124I PET dosimetry protocol for radioiodine therapy of differentiated thyroid cancer *J. Nucl. Med.* **49** 1017–23
- Kamphuis C, Beekman F J, van Rijk P P and Viergever M A 1997 Dual matrix ordered subsets reconstruction for accelerated 3D scatter compensation in single-photon emission tomography *Eur. J. Nucl. Med. Mol. Imaging* **25** 8–18
- Laforest R, Rowland D J and Welch M J 2002 MicroPET imaging with nonconventional isotopes *IEEE Trans. Nucl. Sci.* **49** 2119–26
- Le Loirec C and Champion C 2007a Track structure simulation for positron emitters of medical interest. Part I: the case of the allowed decay isotopes *Nucl. Instrum. Methods Phys. Res. A* **582** 644–53
- Le Loirec C and Champion C 2007b Track structure simulation for positron emitters of physical interest. Part II: the case of the radiometals *Nucl. Instrum. Methods Phys. Res. A* **582** 654–64
- Le Loirec C and Champion C 2007c Track structure simulation for positron emitters of physical interest. Part III: the case of the non-standard radionuclides *Nucl. Instrum. Methods Phys. Res. A* **582** 665–72
- Levin C S and Hoffman E J 1999 Calculation of positron range and its effect on the fundamental limit of positron emission tomography system spatial resolution *Phys. Med. Biol.* **44** 781–99
- Li J and Koral K 2007 Nature of ringing artifacts in SPECT reconstruction and their reduction by the use of side information *2007 4th IEEE Int. Symp. on Biomedical Imaging: From Nano to Macro (IEEE)* pp 181–4
- Lubberink M 2001 *Quantitative Imaging with PET: Performance and Applications of 76Br, 52Fe, 110mIn and 134La* (Uppsala University)
- Lubberink M and Herzog H 2011 Quantitative imaging of 124I and 86Y with PET *Eur. J. Nucl. Med. Mol. Imaging* **38** 10–18
- Lubberink M, Schneider H, Bergstr M M and Lundqvist H 2002 Quantitative imaging and correction for cascade gamma radiation of 76Br with 2D and 3D PET *Phys. Med. Biol.* **47** 3519–34
- Ogawa K, Harata Y, Ichihara T, Kubo A and Hashimoto S 1991 A practical method for position-dependent Compton-scatter correction in single photon emission CT *IEEE Trans. Med. Imaging* **10** 408–12
- Ouyang J, El Fakhri G and Moore S C 2007 Fast Monte Carlo based joint iterative reconstruction for simultaneous SPECT imaging *Med. Phys.* **34** 3263–72
- Pandya D N, Bhatt N B, Almaguel F, Rideout-Danner S, Gage H D, Solingapuram Sai K K and Wadas T J 2019 89Zr-chloride can be used for immuno-PET radiochemistry without loss of antigen reactivity *in vivo* *J. Nucl. Med.* **60** 696–701
- Phuong Nguyen M, Oostenrijk B, Kamphuis C and Beekman F J 2022 Ultra-high sensitivity simultaneous small animal PET-SPECT for microCi range imaging *J. Nucl. Med.* **63** 2344
- Rahmim A, Qi J and Sossi V 2013 Resolution modeling in PET imaging: theory, practice, benefits, and pitfalls *Med. Phys.* **40** 064301
- Rinne S S, Abouzayed A, Gagnon K, Tolmachev V and Orlova A 2021 66Ga-PET-imaging of GRPR-expression in prostate cancer: production and characterization of [66Ga]Ga-NOTA-PEG2-RM26 *Sci. Rep.* **11** 3631
- Rosar F et al 2021 Impact of prompt gamma emission of 44Sc on quantification in preclinical and clinical PET systems *Appl. Radiat. Isot.* **170** 109599
- Rosch F, Herzog H, Plag C, Neumaier B, Braun U, Muller-Gartner H-W and Stocklin G 1996 Radiation doses of yttrium-90 citrate and yttrium-90 EDTMP as determined via analogous yttrium-86 complexes and positron emission tomography *Eur. J. Nucl. Med.* **23** 958–66
- Sibczynski P et al 2017 Characterization of some modern scintillators recommended for use on large fusion facilities in γ -ray spectroscopy and tomographic measurements of γ -emission profiles *Nukleonika* **62** 223–8
- Tong S, Alessio A M, Thielemans K, Stearns C, Ross S and Kinahan P E 2011 Properties and mitigation of edge artifacts in PSF-based PET reconstruction *IEEE Trans. Nucl. Sci.* **58** 2264–75

- Topping G J, Schaffer P, Hoehr C, Ruth T J and Sossi V 2013 Manganese-52 positron emission tomography tracer characterization and initial results in phantoms and *in vivo* *Med. Phys.* **40** 042502
- Tuy H K 1983 An inversion formula for cone-beam reconstruction *SIAM J. Appl. Math.* **43** 546–52
- Vaissier P E B, Beekman F J and Goorden M C 2016 Similarity-regulation of OS-EM for accelerated SPECT reconstruction *Phys. Med. Biol.* **61** 4300–15
- Vaissier P E B, Goorden M C, Vastenhouw B, van der Have F, Ramakers R M and Beekman F J 2012 Fast spiral SPECT with stationary γ -cameras and focusing pinholes *J. Nucl. Med.* **53** 1292–9
- Vastenhouw B and Beekman F 2007 Submillimeter total-body murine imaging with U-SPECT-I *J. Nucl. Med.* **48** 487–93
- Villena J L, Tapias G, Lage E, Kreuger R and Beekman F J 2010 Evaluation of a 25-511keV list mode readout system for a large field-of-view gamma camera *IEEE Nuclear Science Symp. & Medical Imaging Conf.* (IEEE) pp 2168–73
- Walrand S, Jamar F, Mathieu I, Camps J, Lonneux M, Sibomana M, Labar D, Michel C and Pauwels S 2003 Quantitation in PET using isotopes emitting prompt single gammas: application to yttrium-86 *Eur. J. Nucl. Med. Mol. Imaging* **30** 354–61